TECHNICAL PAPER

Estimation of Tensile Properties of Pressure Vessel Steel Through Automated Ball Indentation and Small Punch Test

S. Arunkumar[1] · Raghu V. Prakash[1]

Abstract Extraction of mechanical properties of in-service materials through small specimen test techniques has become attractive in the recent years. Of the available small specimen test techniques, automated ball indentation (ABI) and small punch test (SPT) methods have proved to be more promising. These test methods are basically non-destructive in nature and are proficient enough to extract the flow properties of the materials using small volume specimen. In this work, tensile properties of a pressure vessel steel (P12) have been estimated through ABI and SPT. The objective is to compare the capability of these test methods in determining the tensile properties. The influence of lubrication (between the indenter and the specimen) on the ABI response is also investigated. The ABI response is found to be similar and the effect on the tensile properties was under 2 %. The tensile properties estimated from ABI and SPT are found to be in good agreement with conventional tensile test results. Nevertheless, in case of SPT, the error in the estimation of yield strength and ultimate tensile strength using empirical correlations is significantly high. However, the use of analytical formulations to convert the SPT load–displacement response to stress–strain curve are found to be reliable, since the error in the estimated properties is considerably less. The ABI process is numerically simulated to study the stress–strain field beneath the indenter. The maximum strain occurs at the edge of the contact indicating the material displacement along the radial direction. The plastic zone beneath the indenter resemble hemispherical shape which is in agreement with the expanding cavity model. The nature of stress changes from compressive (right below the indentation axis) to tensile at the edge of contact. This indicates that radial cracks may initiate on the specimen and propagate outwards. The pile-up is significantly higher in the case of frictionless contact between the indenter and the specimen but found to converge for a value of around 0.2.

Keywords Indentation · Pile-up · Tensile properties · Small punch test · Numerical simulation

1 Introduction

Estimation of tensile properties of materials like, elastic modulus, yield strength and strain hardening exponent is considered to be of fundamental importance. Basically, these properties are measured by standard tensile tests, such as ASTM E-08 M [1]. These test methods are destructive in nature and require reasonable specimen cross-section and volume. There are situations where limited volume of material is available for property assessment, like in material development, failure analysis and remaining life assessment of in-service components. In these situations, test techniques using small volume specimens become more attractive. Small specimen test techniques have been established as a reliable alternative to traditional tensile test, as the results of these test techniques are in good agreement with the tensile test and are reproducible when tested under controlled conditions. Of the available small specimen test techniques, automated ball indentation (ABI) is widely used due to its capability to extract the flow properties of various material systems like bulk, functionally graded and prior damaged materials [2–

✉ Raghu V. Prakash
raghuprakash@iitm.ac.in

[1] Indian Institute of Technology Madras, Chennai, Tamilnadu, India

6]. This test technique is non-destructive in nature and can be used for in situ examination of mechanical properties. ABI involves indenting the specimen with a spherical ball in few steps of incremental loading and unloading (typically five or seven); load versus depth of penetration is continuously monitored during this incremental loading. However, this technique may not be feasible for samples whose thickness is less than ∼1 mm, typical of scooped samples. In this situation, an alternative testing method can be the small punch test (SPT), and it is capable of extracting flow properties of samples with size <1 mm thick. SPT can also be used for extracting creep, fatigue and fracture properties of materials [7–10].

In SPT, a thin sample, clamped between the two circular dies, is bi-axially loaded till failure; load vs. displacement response is monitored during the stretching process. In both the test methods (viz., ABI and SPT) the recorded load-depth curve is converted into stress–strain response with the available correlations reported in the literature [11–20]. Despite the inherent merits of these test techniques, an understanding of their capability enables one to confidently adopt them for the extraction of tensile properties. In this regard, the tensile properties of pressure vessel steel, P12, estimated by ABI and SPT are compared with the standard tensile test results. It has been reported in the literature that, the properties determined by ABI are affected by an error associated with the contact radius measurement. This may be due to the so called, pile-up/sink-in phenomena. The two factors that influence the pile-up/sink-in phenomena are: (i) strain hardening exponent of the specimen and (ii) friction coefficient between the indenter and the specimen. The effect of these two parameters on the amount of pile-up/sink-in has already been understood [21]. However, for a given material, it is necessary to study the influence of lubrication between the indenter and the specimen, on the load-depth curve and its effect on the assessed properties. In this work, the contact surface was lubricated with SAE 40 oil and Molybdenum-di-sulphide (MoS₂) grease to investigate its effect on the load-depth response and tensile properties.

During indentation, the specimen may be subjected to elastic, elastic–plastic and fully plastic deformation [22]. For elastic deformation, Hertz obtained theoretical solution for stress and displacement fields. However, in reality, for very small penetration depths, the contact remains elastic. As the plasticity develops beneath the indenter at larger depths, the theoretical analysis of stress-displacement field becomes cumbersome due to uncertainty about the evolution of the plastic zone [23]. Using finite element method, the evolution of plastic zone and the stress field beneath the indenter can be captured. Several models have been proposed about the nature and extent of the deformation zone beneath the sharp indenters in terms of slip

line field, elastic displacements and compression mechanism [24–26]. Of these models, the most accepted is the compression mechanism. In this model, the deformation zone beneath the indenter is approximated to radial compression of hemispherical shells (which is similar to expansion of hemispherical cavity) with a cap of dead metal (high strain cap) around the first point of contact of the sharp indenter. The presence of friction makes the cap of dead metal to adhere to the tip of the indenter and thus altering the deformation mode. Johnson [27] replaced this high strain cap with a core subjected to hydrostatic internal pressure. With this correction to the model, the prediction of stress–strain curve is found to be reasonably in good agreement with the experimental results. The model also claims that the probability of stress pattern being affected by indenter shape (spherical or sharp) is very less. In this context, an attempt is made to simulate the ABI process to examine the evolution of the plastic zone and stress field beneath the indenter under elastic–plastic indentation and to verify whether the deformation zones resemble the hemispherical shells as approximated by the expanding cavity model.

The typical load-depth response of ball indentation test and the geometry of indentation is presented in Fig. 1. Loubet et al. [28] were the first to indicate that the initial unloading portion of load-depth response is elastic in nature. Later, Oliver and Pharr [15] proposed that the unloading slope from the initial linear portion of the unloading curve can be used to extract the elastic modulus of the material. Haggag proposed a set of semi-analytical equations through which the plastic properties like yield strength, strength coefficient, strain hardening exponent and ultimate tensile strength can be estimated by an iterative procedure, which is described elsewhere [29].

In case of SPT, a thin sample clamped between two circular dies, is stretched untill complete failure, using a hemispherical head punch. The typical load–displacement response of SPT is presented in Fig. 2 and it may be interpreted as follows:

Region I Linear elastic—The entire specimen undergoes elastic bending deformation which is linear. This portion of the curve is governed by Young's modulus and Poisson's ratio.
Region II Plastic bending—This stage is a transition from elastic to plastic deformation which is mostly governed by the strength coefficient, K and strain hardening exponent, n. The material behavior departs from linearity with a slope change due to yielding.
Region III Membrane stretching—The slope of the load–displacement response further increases in this phase due to work hardening. The specimen undergoes membrane stretching due to the biaxial stresses.
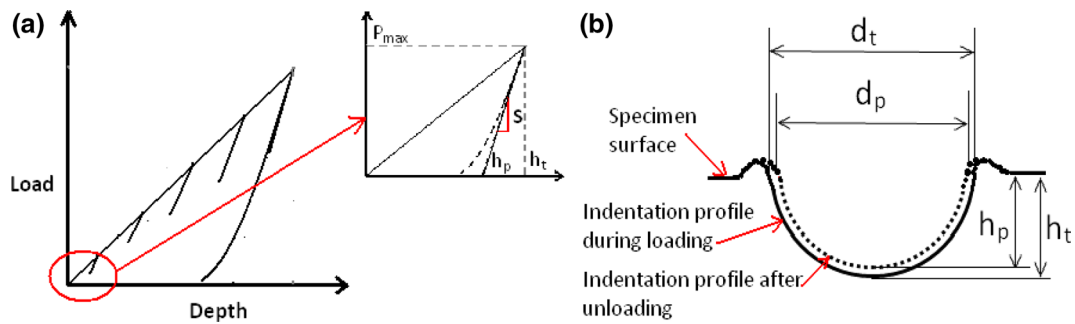
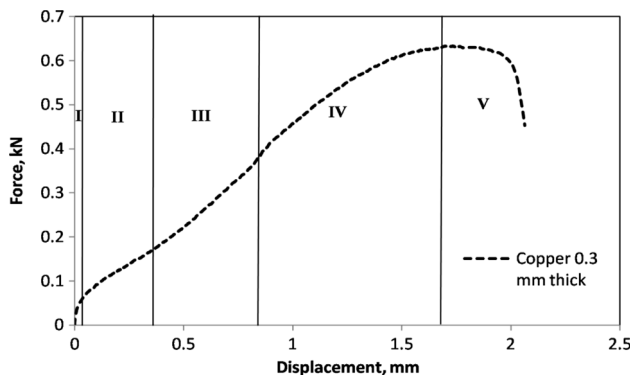Fig. 1 a Load-depth response. b Geometry of indentation profile

Fig. 2 Deformation regimes of small punch test [34]

Table 1 Material composition (% weight)

C	Mn	Si	S	P	Cr	Ni	Mo
0.08	0.4	0.5	0.025	0.025	1.2	–	0.52

Region IV Plastic instability—In this stage the material softening and damage starts with void nucleation and coalescence. A considerable reduction in the thickness of the specimen may be observed in this portion of deformation regime.

Region V Fracture zone—During this stage the specimen fails by circumferential crack propagation with a simultaneous drop in the load.

This load–displacement response is then converted to stress–strain curve using the correlations available in the literature. In this work, the elastic modulus, yield strength and ultimate tensile strength (both empirical and analytical correlations), and plastic properties are evaluated using the equations described elsewhere respectively [30–33].

2 Experimental Method and Material

2.1 Automated Ball Indentation

The material used for ABI and SPT is P12 steel whose composition is presented in Table 1. The sample was polished with 800, 1000, and 1200 grit emery papers to diminish the influence of surface irregularities during indentation.

Indentation experiments were performed using a MTS 810 servo hydraulic test system. A spherical ball made of tungsten carbide (WC) of diameter 1.5875 mm (1/16″) was used. A displacement gauge (full range: ± 3 mm) was mounted between the knife edges of the loading members, to measure the local displacement of the indenter. The force and displacement transducers were scaled down to 1/10th of its full range (LVDT FSR: ± 75 mm and Load Cell FSR: ± 100 kN) for the indentation experiments. The tests were carried out under displacement control mode. The data was acquired at the rate of 20 Hz. The schematic of the fixture and experimental set up is shown in Fig. 3. The results presented in this work are the average of 3 test trials.

2.2 Small Punch Test

SPT was conducted on P12 steel of 0.3 mm thick (nominal) samples. Figure 4 presents the schematic and photograph of test set up and fractured SPT sample. The samples were carefully polished and placed in between the dies and clamped using the screws. The clamp pressure on the specimen was controlled using a torque wrench. A tungsten carbide ball of diameter 2.5 mm was then placed on the specimen. The punch was inserted through the guide hole; the whole test fixture was then placed between the hydraulic grips of MTS servo-hydraulic test system using compression plates (flat rigid plates) to ensure uniform load transfer from the test system to the punch. The local displacement of the specimen was measured using a crack opening displacement gauge mounted on to the knife edges of the dies. The force and displacement transducers were scaled downed to 1/10th of its full range for the SPT experiments. The load–displacement data was continuously recorded at a rate of 20 Hz. Test was repeated at least 3

times to ensure repeatability of estimated properties. Both ABI and SPT tests were carried out at room temperature, lab air conditions i.e. at 25 °C and approx. 50 % relative humidity (RH).

2.3 Numerical Procedure and Experimental Validation

ABI test was simulated using ABAQUS® standard finite element software. The indenter and the specimen were modeled as 2D axi-symmetric deformable bodies in order to minimize the computational time. The constitutive behavior of the material used in this analysis was linear elastic and rate dependent plastic with isotropic hardening conforming to the von-Mises yield criterion. The true stress-true strain data was obtained from tensile test and used as an input to the simulation (Fig. 5). The boundary conditions imposed on the model were: (i) the axial displacement of the specimen was fixed at the bottom surface (ii) the translation (along X direction) and rotation (along Z direction) of the indenter and the specimen along the axis

of symmetry were constrained. It may be noted that many investigators in the literature have used rigid indenter as the basis for ABI simulations. In fact, practically, there is no such thing called as 'rigid' indenter and it is a computational approach used for modeling. As per Ref. [20], for a valid indentation test, both under static and dynamic conditions, the ball hardness should be at least twice the hardness of the test material. The modulus of the indenter in the present case was nearly three times greater than that of the specimen, which implied that for a given stress, even the indenter could deform by a small amount equal to one-third the indented material's deformation even under purely elastic conditions of loading. Further, it was noted through our earlier studies that the assumption of rigid indenter provided an approximate 15 % over estimation of experimental response compared to deformable indenter. Thus, to simulate the testing conditions as closely as possible, the indenter was modeled as a deformable body.

The indenter penetrated the specimen under displacement control mode. Contact conditions were defined for
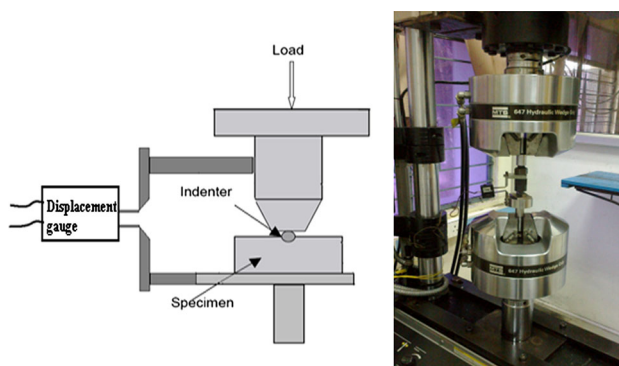

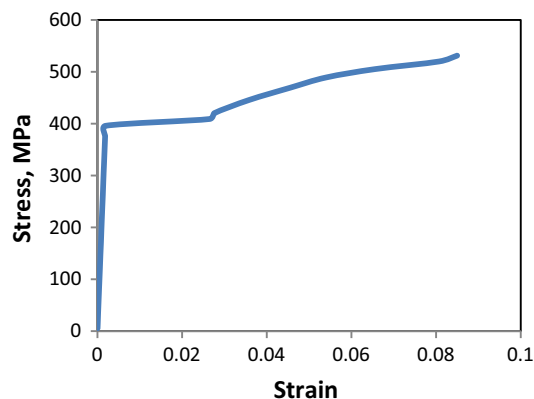**Fig. 3** Schematic and photo of ABI test set up

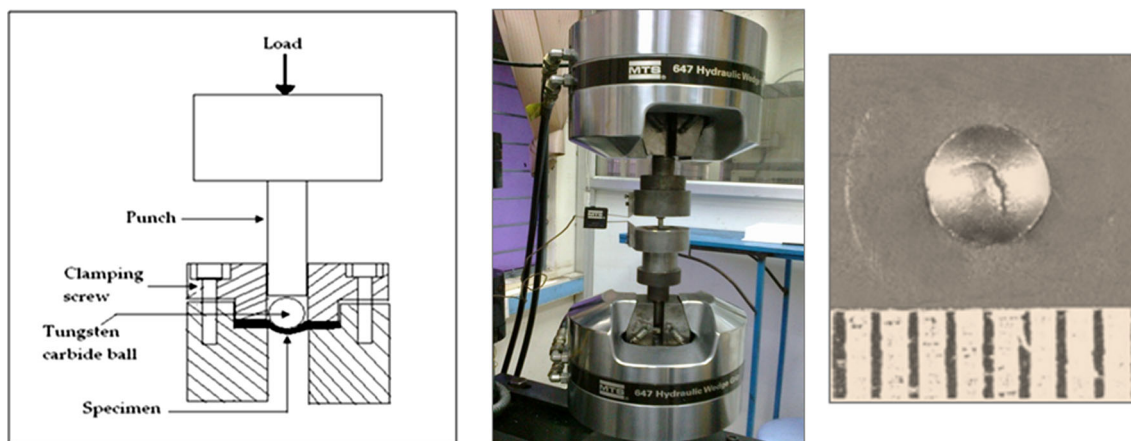**Fig. 5** Stress–Strain curve obtained from tensile test

Fig. 4 Schematic and photo of small punch test set up and Fractured SPT sample

both the indenter and the specimen by using coulomb's friction model. The indenter was defined as master surface and the specimen as slave surface. Surface-to-surface discretization was used for better convergence. The entire model was meshed with CAX8R - An 8-node bi-quadratic axi-symmetric quadrilateral, reduced integration element suitable for analyzing large stress and strain gradients and contact interaction problems [30]. The mesh at the vicinity of the contact was made finer while it was coarser away from the contact zone, to reduce the computational time and memory (Fig. 6). The number of elements and the contact friction were chosen such that the load-depth response of the numerical model was validated with the experimental results. The deviation of the load-depth response of the finite element model was less than $\sim 8\%$ of the experimental response (Fig. 7). A total of 7607 elements and a coefficient of friction of 0.2 were found to be validated with the experimental response. On comparing the energy outputs, it was revealed that the kinetic energy and artificial energy were zero percent of internal energy.
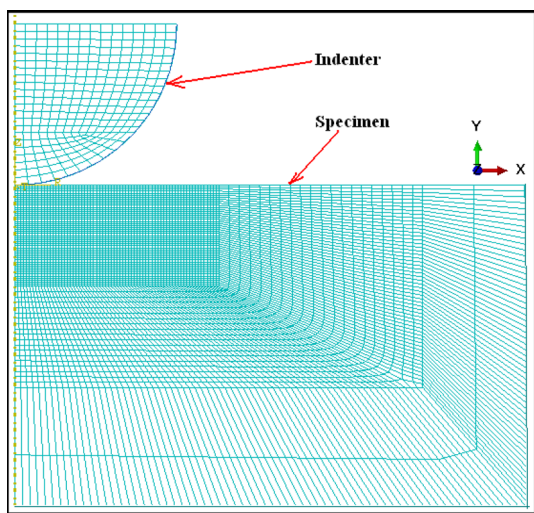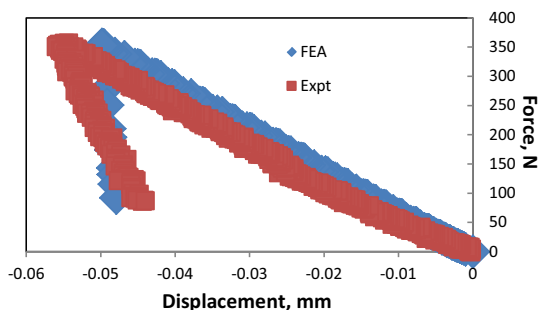
This permitted simulation of the indentation process by static analysis and ensured no hour glass problem [35].

3 Results and Discussion

3.1 Comparison of Tensile Properties

The typical load–displacement response from ABI and SPT is presented in Figs. 8 and 9 respectively. Estimated tensile properties are given in Tables 2 and 3.

The elastic modulus estimated through ABI and SPT are nearly close to that obtained from tensile test. Indeed, the error is less than $\sim 1\%$. The yield strength predicted by ABI is in good agreement with the tensile test result. However, there is a large difference in the yield strength estimated by SPT particularly using empirical formula. The following empirical correlation estimates the yield strength of the sample [30]:

$$\sigma_y = 207 + 0.268\left(\frac{p_y}{t^2}\right) \tag{1}$$

where P_y is the yield load obtained by drawing a line parallel to the linear portion at a distance of (t/10) from the origin and t is the thickness of the sample. This large difference may be attributed to an attempt to draw similarity
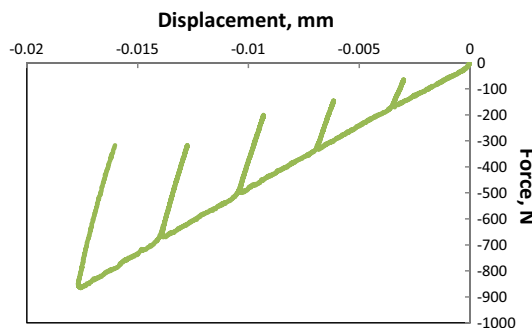

Fig. 6 Meshed geometry of FE model

Fig. 8 Load–depth curve from ABI test

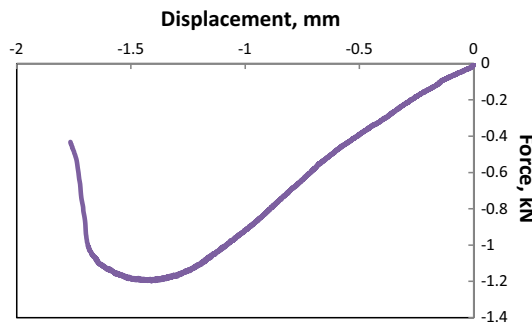Fig. 7 Comparison of load–depth curve of FE model and experiment

Fig. 9 Load–displacement curve from SPT

Table 2 Comparison of tensile properties obtained through conventional tensile test, ABI and SPT

Properties	Tensile test	ABI	Percent deviation w.r.t tensile test (%)	SPT		Percent deviation w.r.t tensile test (%)
Young's modulus (GPa)	206.75	207.54	∼0.4	207.02		∼0.1
Yield strength (MPa)	398	395.95	∼0.5	Empirical	307.84	∼23
				Analytical	434.35	∼9
Ultimate tensile strength (MPa)	531	594	∼12	Empirical	750.04	∼41
				Analytical	594.13	∼12

Table 3 Comparison of strength coefficient and strain hardening exponent by various test methods

Properties	Tensile test	ABI	Percent deviation w.r.t tensile test (%)	SPT	Percent deviation w.r.t tensile test (%)
Strength coefficient (K MPa)	1083.7	1097.6	∼1	1159.85	∼7
Strain hardening exponent (n)	0.2547	0.257	∼0.9	0.2763	∼8

between the small punch and tensile test responses. In case of tensile test, the stress distribution is simple uni-axial and the entire gauge section undergoes full elastic or plastic deformation. As a consequence, a sharp boundary exists between the elastic and plastic deformation in the tensile stress–strain curve. However, in case of SPT the stress distribution and its variation as the test progresses is quite complex and when a part of the specimen yields, the other region is still in elastic state. Hence, it is difficult to find the point in the load–displacement curve of the SPT, where the entire thickness of the sample undergoes yielding either through experiments or by offset/two-tangent method. Thus, estimation of yield load (by offset or two-tangent method) may not be as reliable compared to the values estimated from tensile test, since the stress situations are entirely different in either of the test methods. These methods, namely, offset or two-tangent methods are used to ensure repeatability of the results. In case of offset method, the magnitude of the line that must be offset from the linear portion is not defined clearly—as whether it is t/10 or t/100, where, t is the thickness of the SPT sample. These approximations may result in large error. Moreover, the empirical correlations are basically arrived for a particular class of materials and its applicability for all materials cannot be generalized. In case of analytical formulation, the yield load is obtained by assuming that the tensile surface (free surface/bottom surface) reaches yielding first than the compressive surface (ball-specimen contact surface). However, it raises a doubt whether tensile or compressive surface reaches first yielding, in which case SPT has to be simulated numerically for confirmation. The maximum load obtained from the SPT response is used for calculating the

UTS. However, in tensile test, at the ultimate load, the specimen necks and then fractures. In case of SPT, it is observed that the specimen may thin down and start cracking even before the maximum load is reached [10]. This may lead to a large difference in the UTS estimated by empirical correlation. The following empirical correlation is used to estimate the UTS [30]:

$$\sigma_{UTS} = 286.7 + 0.129(p_{max}/t) \qquad (2)$$

The error is found to be around 41 % as given in Table 2. However, using the following empirical equation, the error can be as high as 77 % [36].

$$\sigma_{UTS} = 269 + 0.051(p_{max}/t^2) \qquad (3)$$

Hence, the estimation of yield and ultimate tensile strengths by empirical correlations from the load–displacement curve seems to be nondeterministic. In case of UTS estimated from analytical formulation, the reason for such a large error may be due to the comparison between the tensile test and SPT. The strength coefficient and strain hardening exponent extracted through ABI and SPT is found to correlate well with the tensile test results. Perhaps, shear punch test provides a fair estimate of UTS values, but it cannot provide true stress-true strain data in the strain hardening region.

The scanning electron microscope (SEM) images of the SPT fractured sample are shown in Fig. 10. The presence of voids on the specimen indicates that the failure of the specimen is due to the coalescence of voids leading the formation of crack during the progression of the test. The fracture surface at higher magnification also shows dimples indicating ductile mode of failure.

3.2 Influence of Lubrication on the ABI Response

The contact surface between the indenter and the specimen was lubricated with SAE 40 and Molybdenum diSulphide (MoS_2) lubricant to understand the effect of lubrication on the ABI response. The tests under lubricated conditions reveals that the load-depth response is nearly similar (Fig. 11). Table 4 reveals the effect of lubrication on tensile properties to be less than $\sim 2\%$ with respect to the dry condition. Examination of the load-depth curve of dry and lubricated cases indicates that, the magnitude of the peak load and the plastic diameter (Table 5) of all cycles is in the following order: $P_{dry} > P_{SAE40} > P_{MoS2}$ and $(d_p)_{Dry} > (d_p)_{SAE40} > (d_p)_{MoS2}$ respectively, for the same displacement of indenter. The plastic diameter under dry condition is higher than the lubricated conditions. This is due the effect of friction, which can be explained as follows: The effect of friction between the indenter and the specimen is to prevent the pile-up of the material. For a strain hardening material, the radial displacement of the material diminishes due to localized hardening at the contact periphery which impedes plasticity at the surface. Thus, the plastic zone is driven deeper into the specimen than radially outward. For the case of SAE40 the plastic diameter is higher than that of MoS_2 indicating that the latter is a better lubricant, as the smaller plastic diameter is an indication of more radial displacement of the material around the indenter. However, in terms of net effect on the true stress-true strain properties, the presence of lubrication does not seem to alter the nature of response, as true plastic strain increases with plastic diameter of penetration, and at the same time, the load required for causing this plastic diameter of penetration also increases depending on the type of lubricated condition. This observation is interesting and reduces the concern regarding the possible distortion in true stress-true strain estimation during ABI testing.

3.3 Numerical Simulation Results

3.3.1 Development of Plastic Zone

The contours of equivalent plastic strain for the three stages of indentation with $(h/R) = 0.01$, 0.02 and 0.03 are presented in Fig. 12a–c. The corresponding values of (a/R) are 0.1, 0.18 and 0.24 respectively. These contours show that the magnitude of plastic strain increases with the depth of indentation. In the early stages of indentation, the maximum plastic strain is close to the indentation axis, while, at higher indentation depths, the same occurs close to the edge of contact with the specimen. This may be due to displacement of the material in the radial direction by the indenter. The flattening shape of plastic strain contours may be observed with progressive indentation. The shape of the maximum strain contour becomes parallel to the specimen surface.

The ratio of plastic zone level in the axial direction (r_{pz}) to radial direction, (r_{pr}), i.e. (r_{pz}/r_{pr}) during loading and unloading is presented in Table 6. The plastic zone is more elongated along the axial direction during the initial stages of indentation while it becomes more rounded i.e. hemispherical at higher indentation depth (Fig. 13). It may be
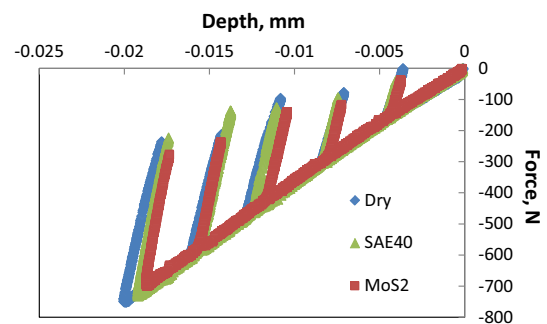
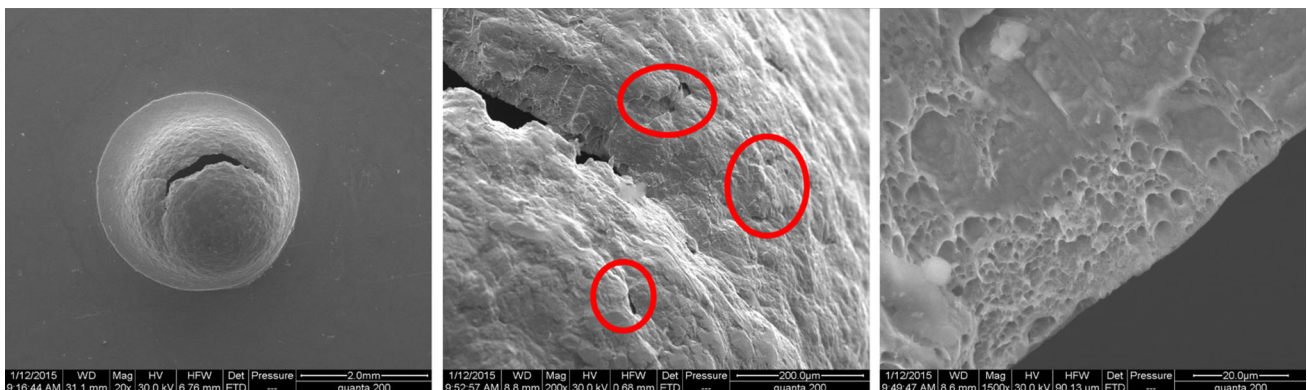**Fig. 11** Effect of lubrication on the ABI load–depth response

Fig. 10 Scannig electron microscope images of SPT fractured sample. The *images* show the presence of voids which gradually grow to a crack. Further examination of fracture surface at higher magnification reveals the presence of *dimples* indicating ductile mode of failure

Table 4 Effect of lubrication on tensile properties of P12 material estimated through ABI

Properties	Dry condition	SAE 40 lubricant	MoS$_2$ lubricant
Young's modulus (GPa)	207.60	208.37	208.63
Yield strength (MPa)	396.42	397.99	397.88
Ultimate tensile strength (MPa)	597.28	598.56	596.64
Strength coefficient (K MPa)	1099.10	1090.60	1085.70
Strain hardening exponent (n)	0.2603	0.2530	0.2520

Table 5 Effect of lubrication on plastic diameters during ABI testing

Test condition		I cycle	II cycle	III cycle	IV cycle	V cycle
Dry	d_p (mm)	0.453435	0.597081	0.715086	0.7889	0.880579
SAE 40	d_p (mm)	0.446665	0.590086	0.705099	0.780799	0.868036
MoS$_2$	d_p (mm)	0.423356	0.570586	0.678348	0.774468	0.850588
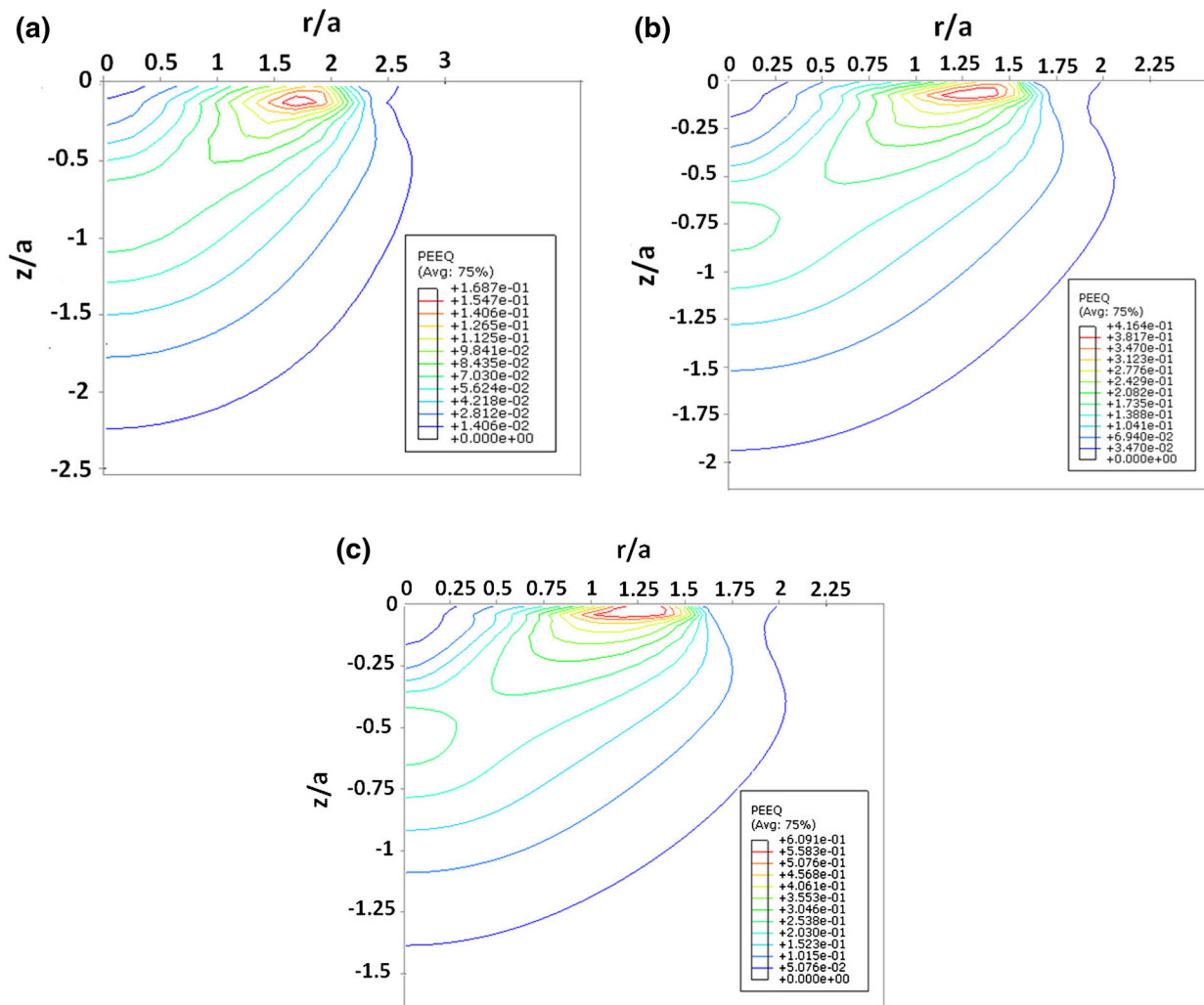
Fig. 12 Contours of equivalent plastic strain at a/R of **a** 0.1, **b** 0.18 and **c** 0.24

Table 6 Ratio of plastic zone aspect ratio (r_{pz}/r_{pr}) for different indentation strains (a/R)

During loading		During unloading	
a/R	r_{pz}/r_{pr}	a/R	r_{pz}/r_{pr}
0.1	1.21	0.10	1.14
0.18	1.12	0.18	0.86
0.24	1.01	0.24	0.74
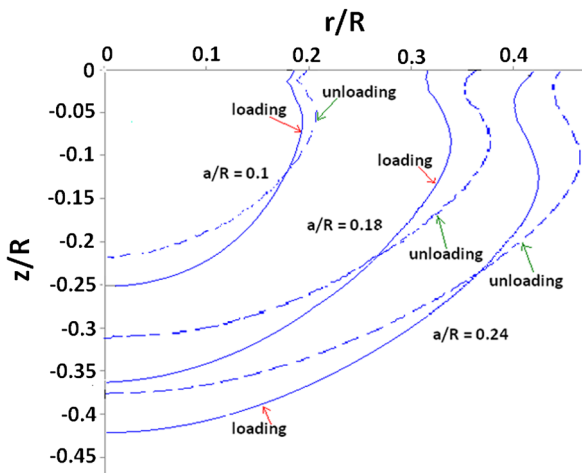
Fig. 13 Development of plastic zone during loading and unloading at different indentation strain, a/R

Fig. 14 Plastic strain distribution along contact zone

Fig. 15 Plastic strain distribution along indentation axis
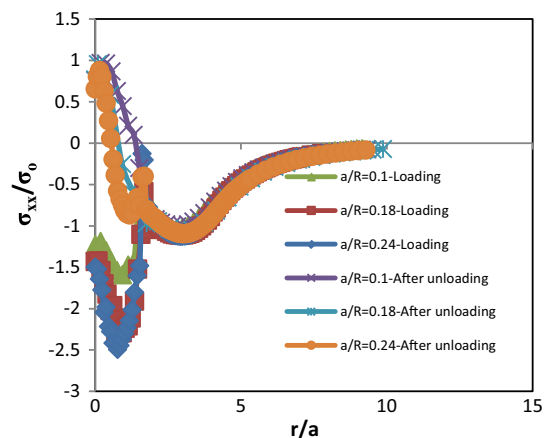
Fig. 16 Distribution of σ_{xx} along contact surface

seen from Table 4 that the ratio r_{pz}/r_{pr} is 1.21 at a/R = 0.1, while it reduces to 1.01 at a/R = 0.24. This indicates that the expanding cavity model which assumes hemispherical shape at larger indentation depths is a plausible approximation.

After unloading, the plastic zone becomes more elongated along the radial direction and shortened along axial direction. This is an indication of material displacement along radial direction.

3.3.2 Equivalent Plastic Strain Distribution

The distribution of equivalent plastic strain along the contact surface and along the indentation axis is presented in Figs. 14 and 15. Along the contact surface, the plastic strain increases from the center of the sphere and attains a maximum value at the edge of contact (which is also observed in Fig. 12). After attaining a maximum value, the strain drops sharply at the edge of contact. Along the indentation axis, the plastic strain reaches its maximum value at the subsurface and then decreases gradually. It may be observed that the location of peak strain at higher indentation depths approaches close to the surface of the specimen.
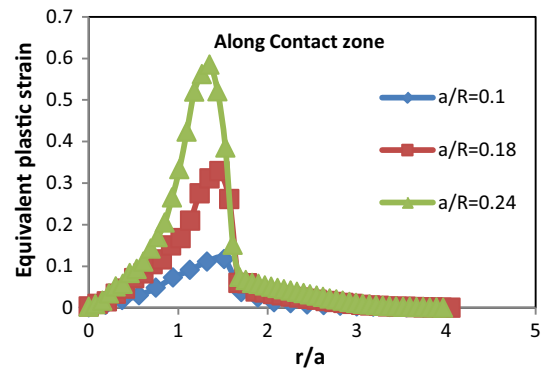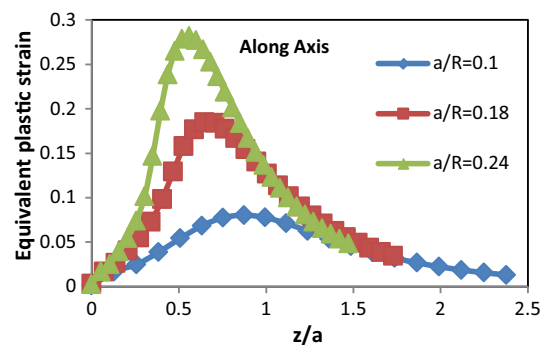
3.3.3 Stress Distribution Along the Contact Zone and Along the Axis

The distribution of stress components, σ_{xx}, σ_{yy}, and σ_{zz} normalized with respect to the yield stress, σ_o for different indentation strains during loading and unloading is
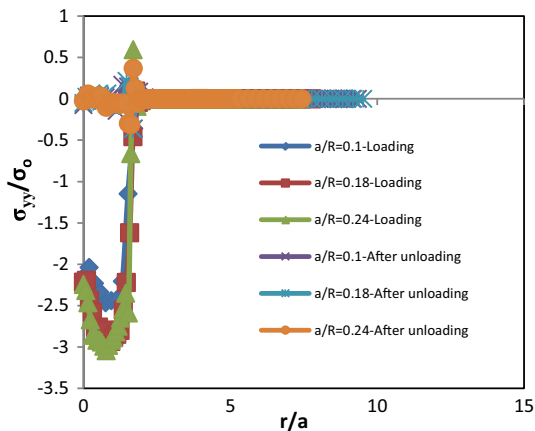

Fig. 17 Distribution of σ_{yy} along contact surface
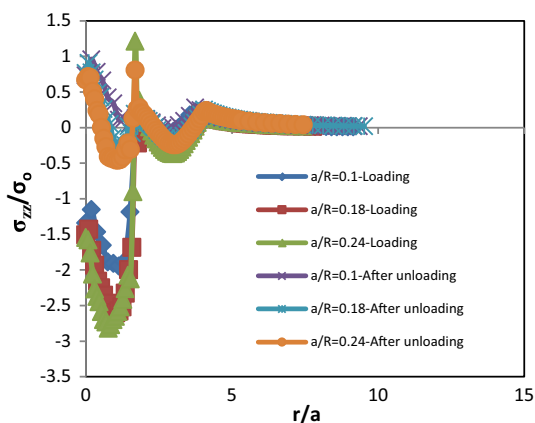

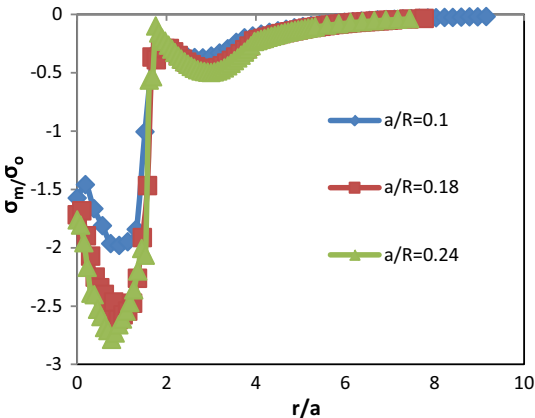**Fig. 18** Distribution of σ_{zz} along contact surface

Fig. 19 Distribution of hydrostatic stress along the contact surface

presented in Figs. 16, 17, 18. It may be observed from these figures that, during loading, the magnitudes of these stress components increases from the point of contact and attain a peak value at the subsurface. Soon after this, there is a sharp drop in these components. It may be seen that the σ_{zz} component is tensile at the edge of contact. This indicates that radial cracks may initiate on the specimen and propagate outwards. The magnitudes of these components are more than two times the yield stress. This may be due to the high magnitude of hydrostatic stress generated beneath the indenter (Fig. 19). Thus, spherical indentation may be used as a test method to study the strain hardening and fatigue response of brittle materials, as the presence of hydrostatic stress delays the fracture to higher strains. After the specimen is unloaded, the tensile residual stresses prevail on the specimen surface.

The variation of normalized stress components with respect to the yield stress is shown in Figs. 20, 21, 22 for different indentation strains during loading and unloading. Right below the point of contact these stress components
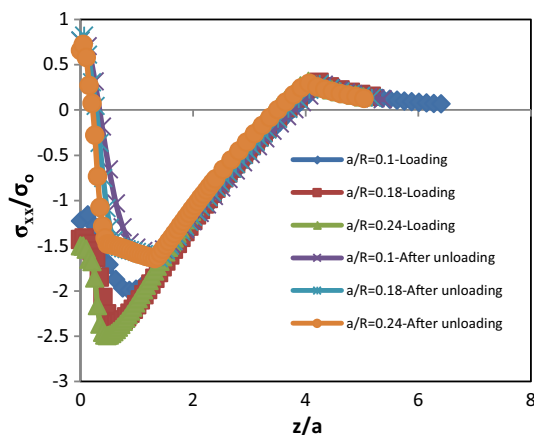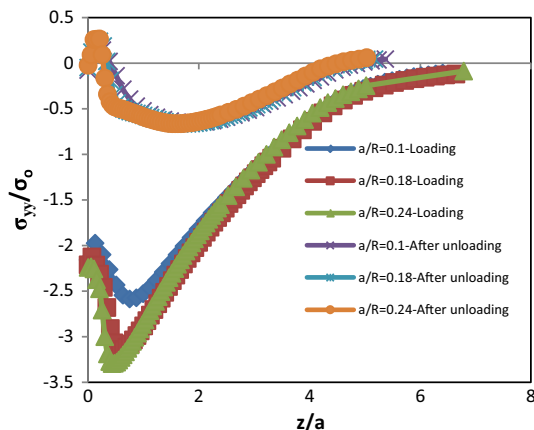

Fig. 20 Variation of σ_{xx} along indentation axis

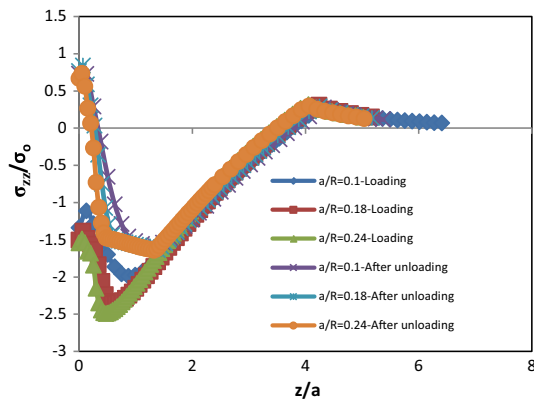**Fig. 21** Variation of σ_{yy} along indentation axis

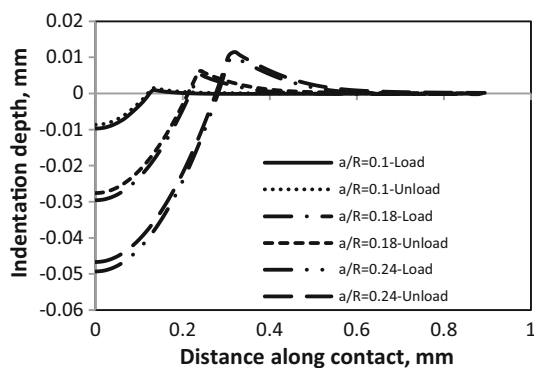**Fig. 22** Variation of σ_{zz} along indentation axis

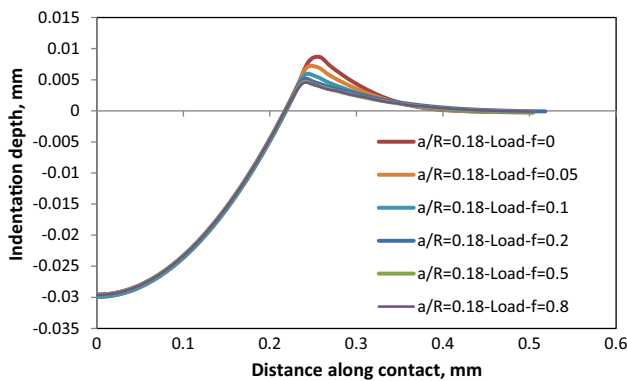**Fig. 23** Pile-up profile at different indentation strains

Fig. 24 Influence of coefficient of friction on the pile-up profile

are compressive and their magnitudes increase at the sub-surface. It may be noted that σ_{xx} and σ_{zz} components become tensile around $(z/a) = 4$.

3.3.4 Influence of friction on the Pile-up profile

The influence of indentation depth and friction coefficient between the indenter and the specimen on pile-up behavior

is presented in Figs. 23 and 24. As the indentation depth increases, the amount of pile-up and the radial displacement of the material increases. The amount of pile-up is quite high for f = 0 and f = 0.05 but it tends to converge at around f = 0.2. A similar observation was also made by Karthik et al. [37]; since, at lower friction, the pile-up is dominant, appropriate correction factors have to be used while estimating the tensile properties [17].

4 Conclusions

Based on the present study, the following observations were made:

1. Tensile properties of the pressure vessel steel, P12 were extracted using ABI and Small Punch Test. The results from either of these test techniques were in good agreement with conventional tensile test. However, in case of SPT, when empirical correlations were used to determine the yield strength and ultimate tensile strength, the error was significantly high. This might be due to the assumption of similarity between the tensile test and SPT and generalization of the empirical correlations which were developed for a specified set of materials.

2. The ABI process was simulated to investigate the stress–strain beneath the indenter. For smaller indentation depths, the maximum strain occurred close to indentation axis while at larger depths, it was close to the edge of contact with the specimen. During the initial stages of indentation, the plastic zone was more elongated along the axial direction, and, it became rounded with increasing depth i.e. hemispherical at higher indentation depth. This is in agreement with the expanding cavity model.

3. The contact stresses wrere compressive in nature beneath the indenter and increased in magnitude from the point of contact and attained a peak value at the subsurface. However, these stresses had a tendency to become tensile at the edge of the contact with specimen which might lead to the formation of radial cracks. Since the presence of hydrostatic stress beneath the indenter postponed the fracture to higher strains, ABI became a favorable test technique for extracting flow properties.

4. The contact friction between the indenter and the specimen was found to have a negligible influence on the tensile properties while it significantly affected the amount of pile-up around the indenter. It was observed that, for frictionless condition, the amount of pile-up was significantly high when compared to higher friction coefficients.

References

1. ASTM E8/E8M-13a, *Standard Test Methods for Tension Testing of Metallic Materials, Annual Book of ASTM Standards*, ASTM International, West Conshohocken, PA (2013).
2. Barbadikar D R, Ballal A R, Peshwe D R, Ganeshkumar J, Laha K, and Mathew M D, *Mater Sci Eng A* **624** (2015) 92.
3. Patil D C, Das M, Das G, Kori S A, and Venkateswarlu K, *Procedia Mater Sci* **5** (2014) 379.
4. Das G, Das M, Sinha S, Gupta K K, Chakrabarty S, and Ray A K, *Mater Sci Eng A* **513–514** (2009) 389.
5. Prakash R V, *Trans Indian Inst Met* **63** (2010) 173.
6. Prakash R V, and Ghosh S, in *Proceedings of the ASTM Symposium on Creep, Creep-Fatigue Interactions*, San Antonio, TX, Nov. 17 (2010).
7. Rasche S, Kuna M, *Int J Press Vessels Pip* **125** (2014) 23.
8. Zhao L, Jing H, Xu L, Han Y, Xiu J, and Qiao Y, *Mater Des* **47** (2013) 677.
9. Eskner M, and Sandstrom R, *J Test Eval* **32** (2004) 11504.
10. Budzakoska E, Carr D G, Stathers, P A, Li H, Harrison R P, Hellier A K, and Yeung, W Y, *Fatigue Fract Eng Mater Struct* **30** (2007) 796.
11. Murty K L, Mathew M D, Wang Y, Shah V N, and Haggag F M, *Int J Press Vessels Pip* **75** (1998) 831.
12. Xu Y, Ning G, Zhang C, Yu Q, and Xu Y, *Int J Press Vessels Pip* **77** (2000) 715.
13. Tabor D, *Proc R Soc Lond Ser A* **192** (1948) 247.
14. Johnson K L, *J Mech Phys Solids* **18** (1970) 115.
15. Oliver W C, Pharr GM, *J Mater Res* **7** (1992) 1564.
16. Herbert E G, Pharr G M, Oliver W C, Lucas B N, and Hay JL, *Thin Solid Films* **398–399** (2001) 331.
17. Talzat B, Zacharia T, and Kosel F, *Int J Solids Struct* **35** (1998) 4411.
18. Haggag F M, in *Small Specimen Test Techniques Applied to Nuclear Reactor Thermal Annealing and Plant Life Extension. ASTM STP 1204*, American Society for Testing and Materials, Philadelphia (1993), p 27.
19. Underwood J H, O'Hara G P, and Zalinka J J *Exp Mech* **26** (1985) 379.
20. Sundararajan G, and Tirupataiah Y, *Bull Mater Sci* **7** (1994) 747.
21. Talzat B, and Pharr G M, *Int J Solids Struct* **41** (2004) 3891.
22. Ahn J-H, and Kwon D, *J Mater Res* **16** (2001) 3170.
23. Fischer-Cripps A C, *J Mater Sci* **34** (1999) 139.
24. Samuels L E, in *Microindentation Techniques in Materials Science and Engineering, ASTM STP 889*, (eds) Blau P J, and Lawn B R, ASTM (1986), p 5.
25. Samuels L E, and Mulhearn T O, *J Mech Phys Solids* **5** (1957) 125.
26. Shaw M C, and DeSalvo D J, *Trans the Am Soc Mech Eng Ser B* **92** (1970) 480.
27. Johnson K L, *J Mech Phys Solids* **18** (1970) 115.
28. Loubet J L, Georges J M, and Meille G, in *Microindentation Techniques in Materials Science and Engineering, ASTM STP889*, (eds) Blau P J, and Lawn B R, American Society for Testing and Materials, Philadelphia (1986), p 72.
29. Haggag F M, in *Small Specimen Test Techniques Applied to Nuclear Reactor Vessel Thermal Annealing Plant Life Extension, ASTM STP 1204*, (eds) Corwin W R, Haggag F M, and Server W L, American Society for Testing and Materials, Philadelphia (1993) p 27.
30. García T E, Rodríguez C, Belzunce F J, and Suárez C, *J Alloy Compd* **582** (2014) 708.
31. Fleury E, and Ha J S, *KSME Int J* **12** (1998) 827.
32. Eskner M, and Sandstrom R, *J Test Eval* **32** (2004), 282.
33. Xu Y, Ning G, Zhang C, Yu Q, and Xu Y, *Int J Press Vessels Pip* **77** (2000) 715.
34. Prakash R V, and Arunkumar S, in *Small Specimen Test Techniques: 6th Volume, STP 1576*, (eds) Sokolov M A, and Lucon E, STP157620140011, ASTM International, West Conshohocken, PA (2014), p 1.
35. Poor H Z, and Moosavi H, *Int J Mech Syst Eng* **3** (2013) 89.
36. Contreras M A, Rodriguez C, Belzunce F J, and Betegon C, *Fatigue Fract Eng Mater Struct* **31** (2008), 727.
37. Karthik V,Visweswaran P, Bhushan A, Pawaskar D N, Kasiviswanathan K V, Jayakumar T, and Raj B, *Int J Mech Sci* **54** (2012) 74.